Chemical Engineering Journal 165 (2010) 64–70

Contents lists available at ScienceDirect

Chemical Engineering Journal

journal homepage: www.elsevier.com/locate/cej

Porous "brick-like" $NiFe_2O_4$ nanocrystals loaded with Ag species towards effective degradation of toluene

Zhengru Zhu [a], Xinyong Li [a,b,*], Qidong Zhao [a], Hong Li [a], Yu Shen [a], Guohua Chen [b]

[a] Key Laboratory of Industrial Ecology and Environmental Engineering (MOE) and State Key Laboratory of Fine Chemical, School of Environmental Science and Technology, Dalian University of Technology, Dalian 116024, China
[b] Department of Chemical & Biomolecular Engineering, The Hong Kong University of Science & Technology, Clear Water Bay, Kowloon, Hong Kong

ARTICLE INFO

Article history:
Received 30 March 2010
Received in revised form 21 August 2010
Accepted 23 August 2010

Keywords:
Chemical co-precipitation
Calcination
Ag loading
Specific surface photovoltage
Photocatalytic degradation

ABSTRACT

Porous and "brick-like" $NiFe_2O_4$ nanoparticles were synthesized by a modified chemical co-precipitation route with calcination temperatures of 773 K, 873 K and 973 K, respectively. The $Ag/NiFe_2O_4$ catalyst was prepared based on the porous $NiFe_2O_4$ by the incipient wetness impregnation strategy, which showed excellent photoelectric property and catalytic activity. The structural properties of these samples were systematically investigated by X-ray powder diffraction (XRD), scanning electronic microscopy (SEM), energy-dispersive X-ray spectra (EDX), UV–vis diffuse reflectance spectroscopy (DRS), and Fourier transform infrared spectroscopy (FT-IR) techniques. The photo-induced charge separation in the samples was demonstrated by surface photovoltage (SPV) measurement. The photocatalytic degradation of toluene by the $Ag/NiFe_2O_4$ and $NiFe_2O_4$ samples was comparatively studied under xenon lamp irradiation. The results indicate that the $Ag/NiFe_2O_4$ sample calcined at 773 K exhibited the highest efficiency for the degradation of toluene.

1. Introduction

Volatile organic compounds (VOCs) are major pollutants usually found in the atmosphere of all urban and industrial areas. A long-term exposure to VOCs is detrimental to human health resulting in sick building syndrome [1,2]. Toluene is one of these compounds. Thus, the development of a "green" treatment process for toluene is greatly desirable. Photocatalysis has been extensively employed for the oxidation of many organic compounds. Recently, increasing attention has been paid to the photocatalytic oxidation of toluene by using visible-light photocatalysts. Obee and Brown reported the influence of the competitive adsorption of water and toluene vapors on the photooxidation rate [3]. Florea et al. reported the photooxidation of toluene on ferrite-type catalysts [4]. Giraudon et al. reported the proper addition of noble metal Pb could increase the catalytic performances for total oxidation of aromatic hydrocarbons [5]. However, the activity and efficiency of these catalysts are not yet satisfying enough to meet the practical needs [4,6,7].

The increasing concern over environmental monitoring and safety demand in industry and home has generated great interest in developing functional materials with unique micro- or nanostructures, as well as fabrication routes of nanomaterials [8–11]. Besides, semiconductor nanocrystals usually exhibit strongly size-, shape-, and crystallinity-dependent electrical properties, which brings innumerous opportunities of obtaining more prominent performance than their bulk form. Cao and coworkers [12] reported the photocatalytic oxidation of toluene by using nanostructured TiO_2 catalysts, but the spectral response was limited to UV region only. From the aspect of solar energy utilization, the exploration of semiconductor photocatalysts of proper band gaps that could utilize visible light efficiently is indispensable.

Ferrite nanoparticles are considered very promising materials that offer several advantages over their metallic counterpart in a variety of applications [13]. Nickel ferrite is one of the most versatile and technologically important ferrite materials because of its typical ferromagnetic properties, low conductivity and thus lower eddy current losses, high electrochemical stability, catalytic behavior and abundance in nature, which crystallizes in a spinel structure and exhibits tunable conducting behavior [14]. Many methods have been developed to prepare nanocrystallite $NiFe_2O_4$ namely sol–gel [15], precipitation [16], hydrothermal [17], combustion [18], mechano-chemical [19], precursor [20] and microemulsion method [21] etc. However, relatively complex schedules, expensive precursors, high reaction temperature and low production rate are

* Corresponding author at: Key Laboratory of Industrial Ecology and Environmental Engineering (MOE) and State Key Laboratory of Fine Chemical, School of Environmental Science and Technology, Dalian University of Technology, No. 2, Linggong Road, Dalian 116024, China. Tel.: +86 411 8470 7733; fax: +86 411 8470 8083.
E-mail address: xyli@dlut.edu.cn (X. Li).

1385-8947/$ – see front matter © 2010 Elsevier B.V. All rights reserved.
doi:10.1016/j.cej.2010.08.060

the common problems. The properties of the synthesized materials are influenced by the composition and microstructure, which are pretty sensitive to the preparation method used in their synthesis. The chemical co-precipitation method is more favorable for its simplicity and good control of grain size in synthesizing magnetic oxides with controlled nanostructures. Their versatile properties derived from various nanostructures still need further comprehensive exploration to achieve a smart system integrated with multi-functions, such as magnetic, photoelectric, photocatalytic and magnetoelectric functions.

Supported noble metal catalysts are widely used in liquid-phase selective alkyne hydrogenation especially for the synthesis of fine chemicals and bio-active compounds [22–24]. The notable advantages of supported noble metal catalysts are relatively high activity, mild process conditions, easy separation, and better handling properties. The commonly used supports for Ag catalysts include activated carbon [25], silica [26–28], alumina [29–31] and zeolite [32]. The choice of an efficient support could significantly improve the activity, selectivity, recycling, and reproducibility of Ag catalyst systems. To fabricate an efficient photocatalyst system, a visible sensitive support for noble metal nanocrystalline catalysts is attractive for achieving higher energy conversion efficiency and photocatalytic activity.

Recently, spinel type oxides like $NiFe_2O_4$ have been used as supports for Ru and Pd catalysts and a distinct metal-support interaction was found [33,34]. Wang et al. [35] have reported on the preparation and magnetic properties of the ferrite timber-like nanocrystal. In this study, porous $NiFe_2O_4$ "brick-like" nanocrystals were fabricated by a modified chemical co-precipitation method along with different annealing temperatures to vary their crystallinity as well as their surface states, then were employed as Ag catalyst supports. After systematic characterization of the bulk and surface structures, their performances in photocatalytic degradation of gaseous toluene were comparatively studied by *in situ* FT-IR spectroscopy.

2. Experimental

2.1. Preparation of catalysts

All the materials were reagent grade and used without further purification. Deionized water was used as a solvent. The "brick-like" $NiFe_2O_4$ nanocrystals were synthesized by a co-precipitation method. 0.1 M (50 mL) aqueous solution of $FeSO_4{\cdot}7H_2O$ and 0.2 M (50 mL) $NiSO_4{\cdot}7H_2O$ were mixed. $Na_2C_2O_4$ solution (0.3 M, 25 mL) was prepared and added to the salt solution. The solution was kept at 353 K and allowed to cool slowly under continuously stirring. A few drops of oleic acid were added to the solution as a surfactant. The precipitate was then washed twice with deionized water and then with ethanol to remove the excess surfactant from the solution. After that, the precipitate was dried overnight at 373 K and the residue water was further removed by heating at 773 K, 873 K and 973 K for 2 h. Then three $NiFe_2O_4$ samples were obtained, named by S1, S2 and S3, respectively.

The catalyst of porous $NiFe_2O_4$ (S1) supported Ag was prepared by a conventional impregnation strategy [36]. $AgNO_3$ solution was used as the precursor. The silver loading was 1 wt.%. After evaporation, the catalyst was then dried at 100 °C for 12 h and calcined at 400 °C in air for 6 h followed by slow cooling under air atmosphere.

2.2. Characterizations

The phase compositions and structures of S1, S2, S3 and Ag/S1 prepared were determined by X-ray diffraction (XRD, RIGAKU, Dmax22000) with Cu Kα radiation (λ = 0.15418 nm) over the 2θ range of 20–80°. The morphology of these samples was investigated by scanning electronic microscopy (SEM) with a JSM-6700 LV electron microscope operating at 5.0 kV and transmission electron microscope (TEM, FEI Tecnai $G^2$20). The compositions were examined by energy-dispersive X-ray spectroscopy (EDX) in the SEM. Light absorption properties were examined using a UV–vis diffuse reflectance spectrophotometer (JASCO, UV-550). The chemical compositions and structures of these samples were determined by a Fourier transform infrared spectrophotometer (BRUKER VERTEX 70 Optics) using KBr pellets.

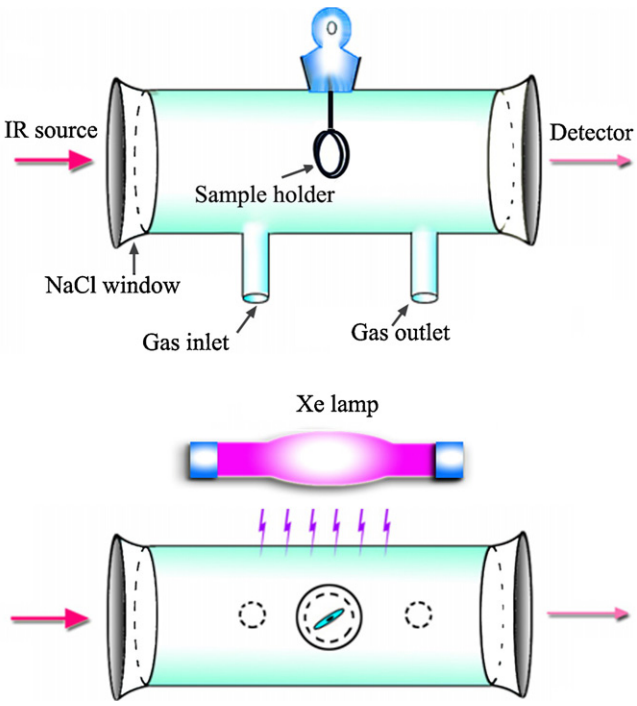

Scheme 1. The schematic diagram of the IR photoreactor.

The characteristics of the photo-generated charge carriers were studied by a lock-in-based surface photovoltage (SPV) measurement system. Lock-in-based surface photovoltage (SPV) measurements were carried out on a home-built system. It consists of a xenon lamp (500 W), a sample cell and a computer-controlled lock-in amplifier (SR830-DSP) with an optical chopper (model SR540) running at 20 Hz. The AC photovoltage signal of the sample was obtained using a capacitor structure. The effective overlapping area of the two electrodes tested here is about 1 cm^2 for all the samples. The samples were pressed into pellets with the same volume and shape for test. The phase spectra were recorded on a computer synchronously with the SPV spectra. All the SPV measurements were operated under ambient conditions and at room temperature.

2.3. In situ FT-IR studies on the photocatalytic performance of $NiFe_2O_4$ and Ag/$NiFe_2O_4$ catalysts

In situ FT-IR spectra were collected with a Fourier transform infrared spectrophotometer (BRUKER VERTEX 70 Optics) and a self-made *in situ* IR quartz photoreaction cell (Scheme 1). The cell had a path length of 10 cm and tubular diameter of 4 cm. Both ends were "capped" by IR-transparent NaCl crystal windows. Approximately the mixture of 30 mg of the $NiFe_2O_4$ sample and 150 mg KBr sample was pressed into a self-supported disk of approximately 13 mm in diameter. The disk was placed in the sample holder (its diameter was about 13 mm) located at the center of the cell. The sample holder was tilted by an angle of 30° with respect to the

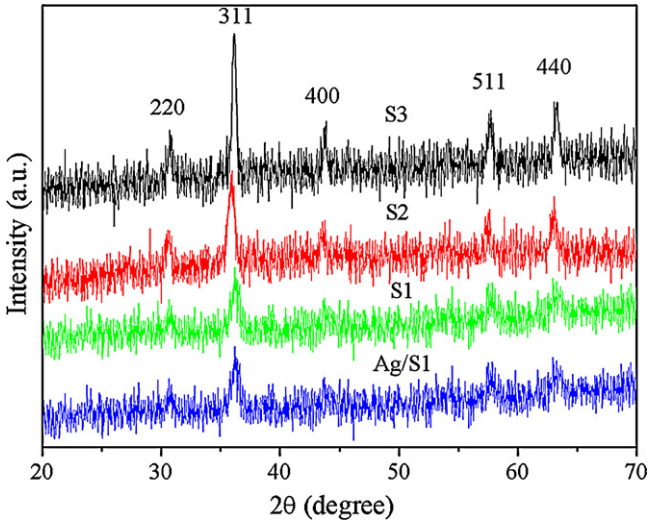

Fig. 1. XRD patterns of S1, S2, S3 and Ag/S1 ferrite samples prepared by the co-precipitation strategy at different calcination temperatures. S1, 773 K; S2, 873 K; S3, 973 K; Ag/S1, 773 K.

IR path. The photocatalyst was illuminated by an XQ-500W xenon lamp. The system configuration is shown by Scheme 1. The distance between the lamp and sample was about 15 cm. The light intensity at the sample holder was about 40.5 mW cm^{-2}. Two wafers were prepared in parallel. The same setup was also used for the wafers of the Ag/$NiFe_2O_4$ sample.

The compressed air used in the reaction was metered (150 mL/min) and pretreated to remove adventitious water or oxygen through three drying columns packed with silica gel, $CaCl_2$, and molecular sieves, respectively. Before illumination, the pre-adsorption equilibrium of toluene on the catalysts was attained by flushing the system with dried toluene species at the flow rate of 2 μL/h for ca. 30 min and then keeping the cell closed for 1 h. The reaction cell was purged by dry air for 1 h. After 1 h, the flux of dry air was set at 20 mL/min. Spectra of the clean catalyst surface were collected after this process and utilized as the background. Subsequently, toluene substrate was fed at a flow rate of 2 μL/h for ca. 30 min by a syringe pump to a mixing tee, where toluene was vaporized and mixed with dry air. The reactant mixture then flowed through the reaction cell and allowed to equilibrate at room temperature (293 K). Once the reactant concentration was stabilized, the inlet and outlet ports were shut off and the lamps were turned on. The infrared spectra were continuously collected during the reaction. After ca. 12 h, the lamps were turned off and the cell was purged with flowing dry air. The infrared spectra were collected with a resolution of 1 cm^{-1} and 20 scans in the region of 4000–600 cm^{-1}.

3. Results and discussion

3.1. The crystalline phase of the samples

The X-ray diffraction patterns (Fig. 1) of S1, S2, S3 and Ag/S1 samples show that the final product is $NiFe_2O_4$ with the inverse spinel structure. Five major characteristic peaks can be indexed as the spinel structure $NiFe_2O_4$, which is accorded well with the reported data (JCPDS File No. 10-0325). The peaks with 2θ values of 30.6°, 36.0°, 44.0°, 57.8° and 63.2°, corresponding to the crystal planes (2 2 0), (3 1 1), (4 0 0), (5 1 1), and (4 4 0) of crystalline $NiFe_2O_4$, respectively. As calculated from the XRD line broadening of the (3 1 1) peak using the Scherrer equation $D = 0.89\lambda/\beta\cos\theta$, the crystallite size was about 10 nm for S1, 14 nm for S2, 21 nm for S3 and 8 nm for Ag/S1. The peak intensity of $NiFe_2O_4$ samples increases with increasing of the calcination temperature, which indicates that the calcination temperature plays a role in the formation of spinel crystal structure and morphology. No peaks corresponding to Ag species could be observed in the X-ray patterns. This may be due to the low content of Ag in the sample.

3.2. The morphology of the samples

The SEM images in Fig. 2 show the morphology of S1 and S3 samples (the images of S2 is similar to S1 and S3, so that its images are not shown). The $NiFe_2O_4$ powders treated under different temperatures are completely composed of "brick"s. The SEM image in high magnification in Fig. 2e indicates that these $NiFe_2O_4$ rods have porous structures. It is also found that the porous "brick-like" of $NiFe_2O_4$ nanocrystals were formed through the agglomeration of numerous nanoparticles. Fig. 2f shows the TEM micrograph of Ag/$NiFe_2O_4$ samples. As indicated by the image, one could hardly distinguish the Ag particles from the support, and hence the EDX patterns of the synthesized Ag/$NiFe_2O_4$ samples were carried out to screen the composition of the metal. Metallic silver was successfully identified by referring to the corresponding EDX patterns of the samples as revealed in Fig. 2g.

3.3. The chemical structures of the samples

Fig. 3a shows the *in situ* FT-IR spectra of S1, S2, S3 and Ag/S1 ferrite samples recorded at room temperature after degassing of oxygen for 2 h, respectively. The band around 600 cm^{-1} corresponds to the intrinsic stretching vibration of metal cations at the tetrahedral site, and the peak at 580 cm^{-1} is attributed to the Fe–O bond vibration of the samples [37,38]. The signals at 3455 cm^{-1}, 1340 cm^{-1} and 1610 cm^{-1} are associated with the stretching vibrations of hydrogen-bonded surface water molecules and hydroxyl groups [35]. All of the bands as appeared in the *in situ* FT-IR spectra of the $NiFe_2O_4$ samples gradually become weaker with increasing of the samples calcination temperature. The results suggest that the calcination process could remove most of the surface hydroxyl groups and adsorbed water.

3.4. UV–vis DRS analysis of the samples

The calcination temperature can affect the patterns of adsorption spectra in the visible-light region (Fig. 3b). It can be also concluded from Fig. 3b that 773 K is a more ideal calcination temperature for obtaining the maximum visible-light absorption over these samples. The highest absorption intensity of Ag/S1 sample was also achieved at this temperature, indicating that the visible-light absorption is closely related to silver loading and the Ag/S1 sample is more sensitive to the visible light than other samples. Therefore, a better photocatalytic capability of the Ag/S1 sample under visible light is assumed.

3.5. Surface photovoltaic analysis of the samples

The SPV method is a well-established non-contact technique for the characterization of semiconductors, which relies on analyzing illumination-induced charges in the surface voltage [39,40]. Fig. 4 shows the SPV spectra of S1, S2, S3 and Ag/S1 samples, respectively. The obtained SPV amplitude and phase spectra for these samples are presented in Fig. 4. It could be observed by systematic comparison of the change of the SPV spectra that the Ag/S1 sample exhibits the most distinguished SPV response, and its performance is evidently higher than all of the other samples. The Ag/S1 sample also shows larger phase retardation with respect to 180°. All of the samples have a similar SPV onset at about 550 nm with tail extending to 800 nm.

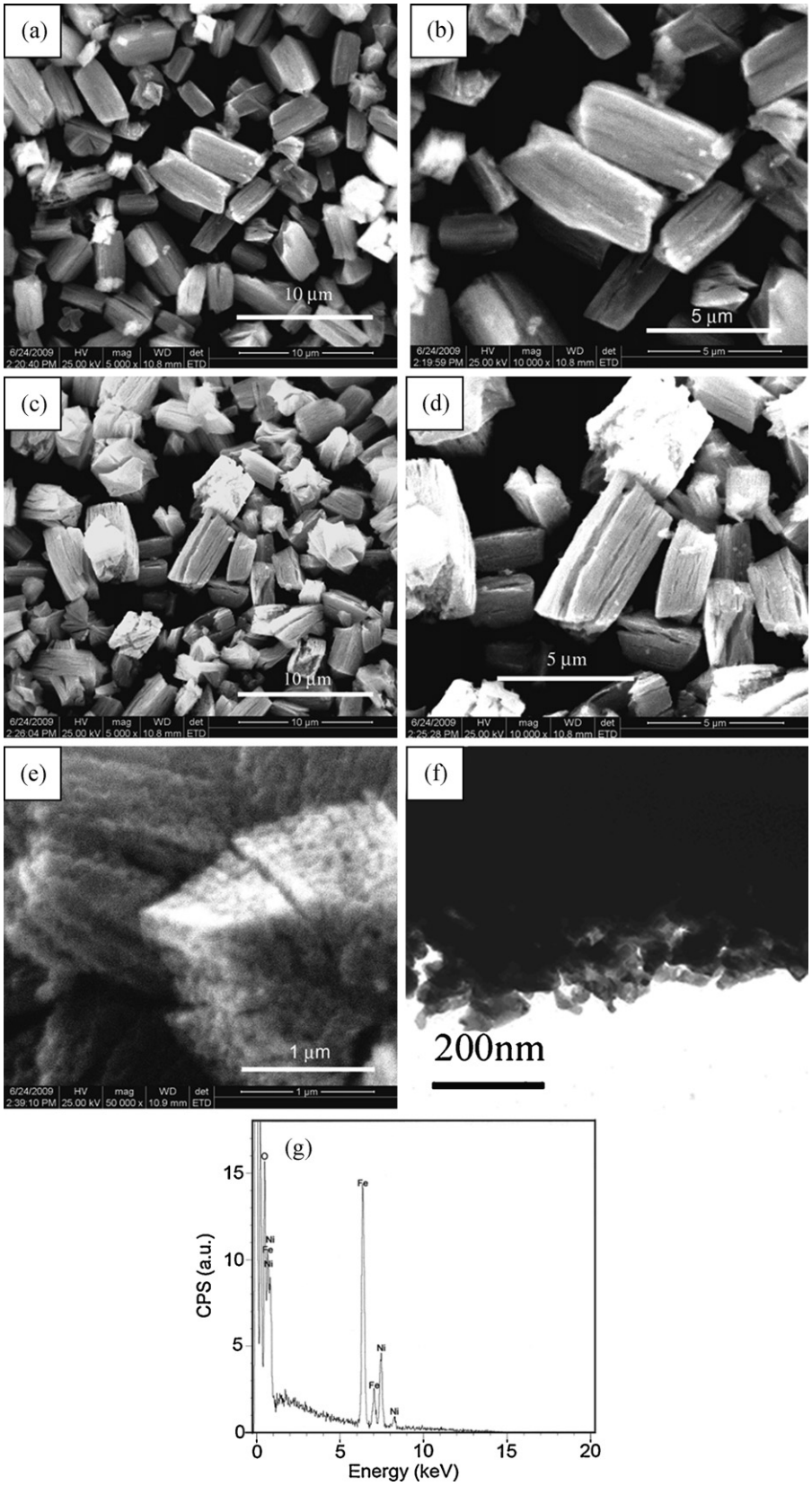

Fig. 2. SEM images of S1 (a, b, e), S3 (c, d) ferrite samples; TEM image of Ag/S1 (f) sample; EDX pattern of Ag/S1 (g) sample.

Unlike the UV–vis spectra, which covers all types of photon absorption, the SPV spectra are only sensitive to the electron transition related process and subsequent charges separation. The corresponding SPV phase value above their band gap is around 90° (Fig. 4, inset), which implies that the photo-generated electrons accumulated at the surface of sample upon excitation [41]. According to the phase value, the diffusion-controlled charge separation dynamics dominates, which means that charge separation

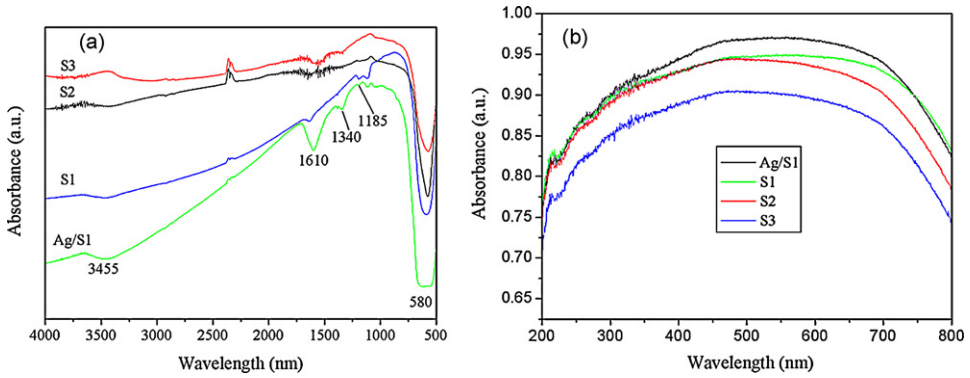

Fig. 3. (a) *In situ* infrared spectra of S1, S2, S3 and Ag/S1 ferrite samples recorded at room temperature after degassing of oxygen for 2 h. (b) UV–vis absorption spectra of S1, S2, S3 and Ag/S1 ferrite samples.

and surface charge accumulation in the sample does not reach equilibrium but increases with time in an illuminating period under the chopped light modulation. The negative sign of the surface photovoltage for these samples is similar to the photo response of a typical p-type semiconductor. Due to the porous structure, the photo-generated electron–hole pairs in the "brick-like" nanocrystal of Ag/S1 are separated mainly via diffusion, rather than by drift. The charge separation efficiency is higher for Ag/S1, as indicated by the much stronger SPV response, thus higher photocatalytic activity might be expected for Ag/S1 sample. Probably, the Ag species adsorbed onto the surface of $NiFe_2O_4$ play a key role in trapping the photo-generated electrons, which is due to that the Fermi level of Ag (ca. −4.3 eV) [42] is much lower than the conduction band edge of the $NiFe_2O_4$ nanocrystals in electronic energy [43].

3.6. The photocatalytic activity and photocatalytic mechanism of the samples

Fig. 5a shows the photocatalytic oxidation of toluene over Ag/S1, S1, S2, and S3 samples, after the reaction proceeding for 12 h under xenon lamp irradiation conditions. It is obviously seen that the Ag/S1 sample is more active than other samples, and the Ag/S1 catalyst shows the highest photocatalytic activity.

In order to test the stability of Ag/S1 catalyst under repeated photocatalytic cycles, more experiments were carried out under the same *in situ* FT-IR test condition (Fig. 5b). Every repetition experiment was carried out up to 6 h. The ratio of photodegradation was measured as a function of time for Ag/S1 catalyst. The results are shown in Fig. 5b. It is found that the conversion ratio gradually decreases with growing photocatalytic degradation cycles. After the fourth repetition, the photodegradation ratio reaches to 34.3% (much lower than the first degradation cycle), and the catalyst must be deactivated at the time. Then the catalyst was calcined at 773 K for 2 h for its regeneration. The degradation ratio over the calcined Ag/S1 catalyst reached to 79.7% after 6 h light irradiation, which is similar to that (80.9%) with the fresh Ag/S1 catalyst. The results show that Ag/S1 has good stability and reusability. The deactivated catalyst could be regenerated by removing the surface adsorbates through calcinations. The declined curve slope with increasing reuse cycles should be caused by the adsorbed photocatalytic products on the catalyst surface, which hinder gaseous toluene molecules from adsorption and degradation.

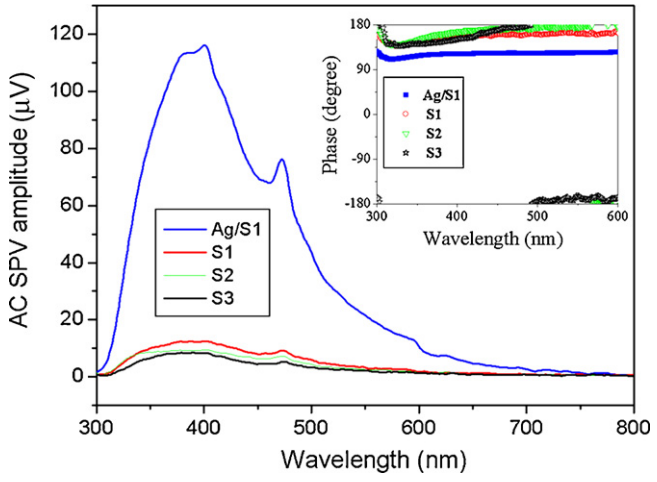

Fig. 4. SPV spectra and corresponding phase spectra (inset) of S1, S2, S3 and Ag/S1 ferrite samples.

As obtained from the *in situ* FT-IR study, the Ag/S1 sample has more hydrogen-bonded surface water molecules and hydroxyl groups adsorbed at its surface due to its smaller crystallite size and higher specific surface area. The surface hydroxyl group would greatly affect the formation of hydroxyl radicals (•OH) since these active species are generated via hole capture by the surface hydroxyl [44,45]. The decreased photocatalytic activity of the samples prepared at higher calcination temperatures should be mainly associated with the reduction of the surface hydroxyls. Thus, Ag/S1 could provide more possibility to form plenty of •OH groups and thus owns higher photocatalytic activity during the photocatalytic process compared with all of the other samples.

We ascribe the mechanism to a synergistic effect between loaded Ag and the porous supports. First, the loaded silver content could not change the band gap of $NiFe_2O_4$, but induce a more intensive absorption band in the visible-light range instead. Hence, we believe that the loaded Ag on the surface of the $NiFe_2O_4$ might be excited by proper incident photons, producing excitons via the plasmon effect [46]. There is a certain possibility that the excitons dissociate. Some of the yielded charges could transfer across the interface between Ag nanoparticle and the $NiFe_2O_4$ support, contributing to the formation of active species at the surface. Secondly, the excited electrons in the CB of $NiFe_2O_4$ would be trapped by Ag species adsorbed onto the surface of $NiFe_2O_4$, and the Ag would enhance the separation of the photo-generated electrons from the holes, which will subsequently help to form active radicals to degrade the adsorbed pollutants.

Compared to the other three samples, the higher separation efficiency of photo-induced electron–hole pairs for the Ag/S1 catalyst was achieved. Additionally, the Ag species adsorbed onto the surface of $NiFe_2O_4$ sample could trap the photo-generated electrons. That is the reason why Ag/S1 catalyst is more active than other samples. In general, the photo-induced holes could be easily captured by chemisorbed surface hydroxyl groups to produce hydroxyl radical groups, i.e., •OH, while the electrons could be

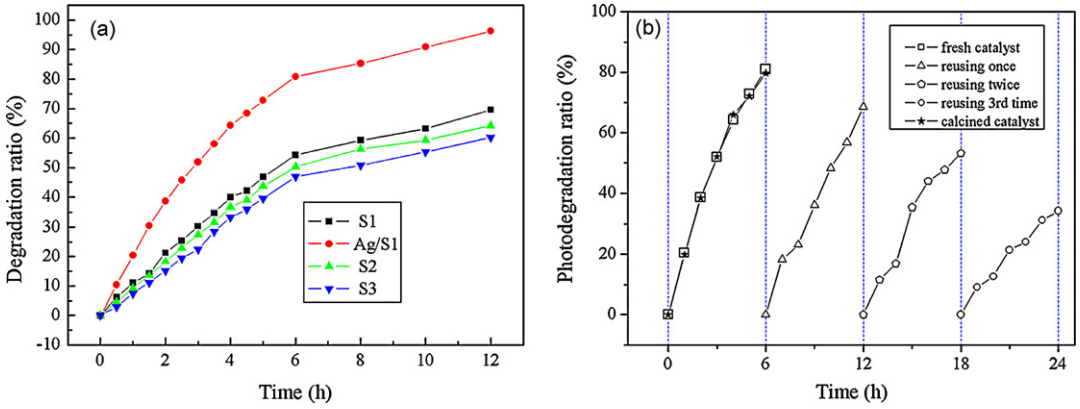

Fig. 5. (a) Degradation percentage of toluene over Ag/S1, S1, S2 and S3 ferrite catalysts under illumination of the xenon lamp with light intensity of 40.5 mW cm^{-2} at the sample. (b) Cyclic photodegradation of toluene by Ag/S1.

trapped by adsorbed O_2^- to produce superoxide radicals, i.e., $\bullet O_2^-$. Both kinds of the radical groups have been shown to be capable of contributing to the oxidation process of organic substances [47]. These results demonstrate that the porous and brick-like nanoparticles of Ag/$NiFe_2O_4$ sample with calcination temperature at 773 K exhibit pretty higher photocatalytic activity.

In situ infrared study provides real-time monitoring of transient events which are occurring on the catalyst during the reaction. In this paper, a set of infrared absorbance spectra obtained during the photocatalytic oxidation of toluene over Ag/$NiFe_2O_4$ nanocrystals are shown in Fig. 6. The spectra were corrected using the clean Ag/$NiFe_2O_4$ nanocrystal as the background. Prior to xenon lamp illumination ($t = 0$), the spectrum displays the characteristic toluene bands at 2920 cm^{-1} and 3028 cm^{-1}, respectively. Upon irradiation, the intensity of these bands begins to decrease slowly. After 12 h prolonged irradiation, the percentage of toluene reaches up to 96.28%, whereas the degradation percentage of toluene over S1, S2 and S3 samples reaches to 69.59%, 64.26% and 60.25%, respectively (see Fig. 5). The responses corresponding to CO_2 (2362 cm^{-1} and 2340 cm^{-1}) and CO (2160 cm^{-1} and 2110 cm^{-1}) increase with reaction proceeding. But the signal corresponding to H_2O (1750–1500 cm^{-1}) is not observed, as water molecular might be absorbed on the wall of the reactor. The photocatalytic oxidation pathways of toluene over S1, S2 and S3 look similar (data not shown). These results show that toluene was mineralized into carbon dioxide and water as the major species, and small amount of carbon monoxide species were also produced during the reactions.

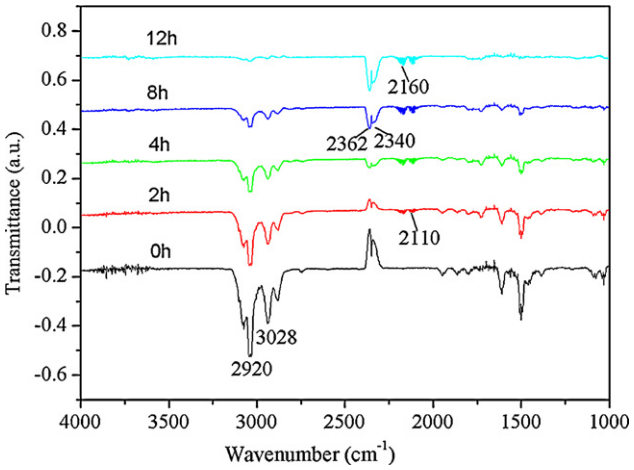

Fig. 6. *In situ* IR spectra taken during the photocatalytic degradation of toluene species at the initial concentration of 750 ppm over Ag/S1 ferrite catalyst for different irradiation time intervals.

4. Conclusions

In summary, the prepared Ag/$NiFe_2O_4$ catalyst with porous and "brick-like" superstructure possesses attractive photovoltage response and remarkable photocatalytic activity in degradation of toluene. The porous $NiFe_2O_4$ catalyst with the brick-like morphology leads to the well dispersion of Ag species on the support, which ensures the access of adsorbates towards the active sites and thus higher catalytic reactivity. The porous "brick-like" Ag/$NiFe_2O_4$ nanoparticles investigated here could be potentially applied in environmental purification and solar energy harvest in the near future.

Acknowledgements

This work was supported financially by the National Nature Science Foundation of China (Nos. 20877013, 20837001), the National High Technology Research and Development Program of China (863 Program) (No. 2007AA061402) and the Major State Basic Research Development Program of China (973 Program) (No. 2007CB613306).

References

[1] H.H. Kim, A. Ogata, S. Futamura, Oxygen partial pressure-dependent behavior of various catalysts for the total oxidation of VOCs using cycled system of adsorption and oxygen plasma, Appl. Catal. B: Environ. 79 (2008) 356–367.
[2] Q.J. Geng, Q.J. Guo, C.Q. Cao, H.Q. Wang, Investigation into photocatalytic degradation of gaseous benzene in a circulated photocatalytic reactor (CPCR), Chem. Eng. Technol. 31 (2008) 1023–1030.
[3] T.N. Obee, R.T. Brown, TiO_2 photocatalysis for indoor air applications: effects of humidity and trace contaminant levels on the oxidation rates of formaldehyde, toluene, and 1,3-butadiene, Environ. Sci. Technol. 29 (1995) 1223–1231.
[4] M. Florea, M. Alifanti, V.I. Parvulescu, D. Mihaila-Tarabasanu, L. Diamandescu, M. Feder, C. Negrila, L. Frunza, Total oxidation of toluene on ferrite-type catalysts, Catal. Today 141 (2009) 361–366.
[5] J.M. Giraudon, A. Elhachimi, F. Wyrwalski, S. Siffert, A. Abouka, Studies of the activation process over Pd perovskite-type oxides used for catalytic oxidation of toluene, Appl. Catal. B: Environ. 75 (2007) 157–166.
[6] R. Schneider, D. Kiessling, G. Wendt, W. Burckhardt, G. Winterstein, Perovskite-type oxide monolithic catalysts for combustion of chlorinated hydrocarbons, Catal. Today 47 (1999) 429–435.
[7] P.O. Thevenin, A.G. Ersson, H.M. Kusar, P.G. Menon, S.G. Jaras, Deactivation of high temperature combustion catalysts, Appl. Catal. A: Gen. 212 (2001) 189–197.
[8] T. Trindade, P. O'Brien, N.L. Pickett, Nanocrystalline semiconductors: synthesis, properties, and perspectives, Chem. Mater. 13 (2001) 3843–3858.
[9] Y. Yin, A.A. Paul, Colloidal nanocrystal synthesis and the organic–inorganic interface, Nature 437 (2005) 664–670.
[10] S. Ayyappan, J. Philip, B. Raj, Effect of digestion time on size and magnetic properties of spinel $CoFe_2O_4$ nanoparticles, J. Phys. Chem. C 113 (2009) 590–596.
[11] N. Bao, L. Shen, W. An, P. Prahallad, C.H. Turner, A. Gupta, Formation mechanism and shape control of monodisperse magnetic $CoFe_2O_4$ nanocrystals, Chem. Mater. 21 (2009) 3458–3468.

[12] L.X. Cao, Z. Gao, S.L. Suib, T.N. Obee, S.O. Hay, J.D. Freihaut, Photocatalytic oxidation of toluene on nanoscale TiO_2 catalysts: studies of deactivation and regeneration, J. Catal. 196 (2000) 253–261.
[13] S. Mitra, K. Mandal, E.S. Choi, Dynamic magnetic properties of $NiFe_2O_4$ nanoparticles embedded in SiO_2 matrix, IEEE Trans. Magn. 44 (2008) 2974–2977.
[14] B. Baruwati, K. Reddy, S. Manorama, R. Singh, O. Parkash, Tailored conductivity behavior in nanocrystalline nickel ferrite, Appl. Phys. Lett. 85 (2004) 2833–2835.
[15] A. Chatterjee, D. Das, S.K. Pradhan, D. Chakravorty, Synthesis of nanocrystalline nickel–zinc ferrite by the sol–gel method, J. Magn. Magn. Mater. 127 (1993) 214–218.
[16] S.G. Doh, E.B. Kim, B.H. Lee, J.H. Oh, Characteristics and synthesis of Cu–Ni ferrite nanopowders by coprecipitation method with ultrasound irradiation, J. Magn. Magn. Mater. 272–276 (2004) 2238–2240.
[17] B. Baruwati, R.K. Rana, S.V. Manorama, Further insights in the conductivity behavior of nanocrystalline $NiFe_2O_4$, J. Appl. Phys. 101 (2007) 014302-1–014302-7.
[18] S. Balaji, R.K. Selvan, L.J. Berchmans, S. Angappan, K. Subramanian, C.O. Augustin, Combustion synthesis and characterization of Sn^{4+} substituted nanocrystalline $NiFe_2O_4$, Mater. Sci. Eng. B 119 (2005) 119–124.
[19] H. Yang, X. Zhang, W. Ao, G. Qiu, Formation of $NiFe_2O_4$ nanoparticles by mechanochemical reaction, Mater. Res. Bull. 39 (2004) 833–837.
[20] X.D. Li, W.S. Yang, F. Li, D.G. Evans, X. Duan, Stoichiometric synthesis of pure $NiFe_2O_4$ spinel from layered double hydroxide precursors for use as the anode material in lithium-ion batteries, J. Phys. Chem. Solids 67 (2006) 1286–1290.
[21] J. Fang, N. Shama, L.D. Tung, E.Y. Shin, C.J. O'Connor, K.L. Stokes, Ultrafine $NiFe_2O_4$ powder fabricated from reverse microemulsion process, J. Appl. Phys. 93 (2003) 7483–7485.
[22] T.A. Nijhuis, G. Koten, J.A. Moulijn, Optimized palladium catalyst systems for the selective liquid-phase hydrogenation of functionalized alkynes, Appl. Catal. A 238 (2003) 259–271.
[23] O. Dominguez-Quintero, S. Martinez, Y. Henriquez, L. D'Ornelas, H. Krentzien, J. Osuna, Silica-supported palladium nanoparticles show remarkable hydrogenation catalytic activity, J. Mol. Catal. A 197 (2003) 185–191.
[24] K.J. Stanger, Y. Tang, J. Anderegg, R.J. Angelici, Arene hydrogenation using supported rhodium metal catalysts prepared from $[Rh(COD)H]_4$, $[Rh(COD)_2]^+BF_4^-$, and $[Rh(COD)Cl]_2$ adsorbed on SiO_2 and Pd–SiO_2, J. Mol. Catal. A 202 (2003) 147–161.
[25] L. Chen, D. Ma, P. Barbara, X. Bao, Carbon-supported silver catalysts for CO selective oxidation in excess hydrogen, J. Nat. Gas Chem. 15 (2006) 181–190.
[26] H. Bi, W. Cai, H. Shi, X. Liu, Optical absorption of Ag oligomers dispersed within pores of mesoporous silica, Chem. Phys. Lett. 357 (2002) 249–254.
[27] X.G. Zhao, J.L. Shi, B. Hu, L.X. Zhang, Z.L. Hua, In situ formation of silver nanoparticles inside pore channels of ordered mesoporous silica, Mater. Lett. 58 (2004) 2152–2156.
[28] J.H. Park, J. Park, H. Shin, The preparation of Ag/mesoporous silica by direct silver reduction and Ag/functionalized mesoporous silica by in situ formation of adsorbed silver, Mater. Lett. 61 (2007) 156–159.
[29] S. Sumiya, M. Saito, H. He, Q.C. Feng, N. Takezawa, K. Yoshida, Reduction of lean NO_x by ethanol over Ag/Al_2O_3 catalysts in the presence of H_2O and SO_2, Catal. Lett. 50 (1998) 87–91.
[30] Y. Yu, H. He, Q. Feng, H. Gao, X. Yang, Mechanism of the selective catalytic reduction of NO_x by C_2H_5OH over Ag/Al_2O_3, Appl. Catal. B: Environ. 49 (2004) 159–171.
[31] E.F. Iliopoulou, A.P. Evdou, A.A. Lemonidou, I.A. Vasalos, Ag/alumina catalysts for the selective catalytic reduction of NO_x using various reductants, Appl. Catal. A: Gen. 274 (2004) 179–189.
[32] C. Shi, M. Cheng, Z. Qu, X. Bao, Investigation on the catalytic roles of silver species in the selective catalytic reduction of NO_x with methane, Appl. Catal. B: Environ. 51 (2004) 171–181.
[33] D. Guin, B. Baruwati, S.V. Manorama, Pd on amine-terminated ferrite nanoparticles: a complete magnetically recoverable facile catalyst for hydrogenation reactions, Org. Lett. 9 (2007) 1419–1421.
[34] B. Baruwati, V. Polshettiwar, R.S. Varma, Magnetically recoverable supported ruthenium catalyst for hydrogenation of alkynes and transfer hydrogenation of carbonyl compounds, Tetrahedron Lett. 50 (2009) 1215–1218.
[35] M. Wang, Z. Ai, L. Zhang, Generalized preparation of porous nanocrystalline $ZnFe_2O_4$ superstructures from zinc ferrioxalate precursor and its superparamagnetic property, J. Phys. Chem. C 112 (2008) 13163–13170.
[36] D.S. Bae, K.S. Han, J.H. Adair, Synthesis and microstructure of Pd/SiO_2 nanosized particles by reverse micelle and sol–gel processing, J. Mater. Chem. 12 (2002) 3117–3120.
[37] B.S. Randhawa, Preparation of ferrites from the thermolysis of transition metal ferrioxalate precursors, J. Mater. Chem. 10 (2000) 2847–2852.
[38] R.K. Selvan, V. Krishnan, C.O. Augustin, H. Bertagnolli, C.S. Kim, A. Gedanken, Investigations on the structural, morphological, electrical, and magnetic properties of $CuFe_2O_4$–NiO nanocomposites, Chem. Mater. 20 (2008) 429–439.
[39] L. Kronik, Y. Shapira, Surface photovoltage phenomena: theory, experiment, and applications, Surf. Sci. Rep. 37 (1999) 1–206.
[40] Q.Z. Zhai, S.L. Qiu, F.S. Xiao, Z.T. Zhang, C.L. Shao, Y. Han, Preparation, characterization, and optical properties of the host–guest nanocomposite material zeolite–silver iodide, Mater. Res. Bull. 35 (2000) 59–73.
[41] V. Donchev, K. Kirilov, T. Ivanov, K. Germanova, Surface photovoltage phase spectroscopy – a handy tool for characterisation of bulk semiconductors and nanostructures, Mater. Sci. Eng. B 129 (2006) 186–192.
[42] S. Ye, L. Fang, Y. Lu, Contribution of charge-transfer effect to surface-enhanced IR for Ag@PPy nanoparticles, Phys. Chem. Chem. Phys. 11 (2009) 2480–2484.
[43] Z. Szotek, W.M. Temmerman, D. Ködderitzsch, A. Svane, L. Petit, H. Winter, Electronic structures of normal and inverse spinel ferrites from first principles, Phys. Rev. B 74 (2006) 174431-1–174431-12.
[44] Y. Ohko, D.A. Tryk, K. Hashimoto, A. Fujishima, Autoxidation of acetaldehyde initiated by TiO_2 photocatalysis under weak UV illumination, J. Phys. Chem. B 102 (1998) 2699–2704.
[45] M.I. Litter, Heterogeneous photocatalysis: transition metal ions in photocatalytic systems, Appl. Catal. B: Environ. 23 (1999) 89–114.
[46] Y. Tian, T. Tatsuma, Mechanisms and applications of plasmon-induced charge separation at TiO_2 films loaded with gold nanoparticles, J. Am. Chem. Soc. 127 (2005) 7632–7637.
[47] X. Chen, S.S. Mao, Titanium dioxide nanomaterials: synthesis, properties, modifications, and applications, Chem. Rev. 107 (2007) 2891–2959.